


 Cite this: *RSC Adv.*, 2023, **13**, 31252

 Received 22nd July 2023  
 Accepted 21st September 2023

 DOI: 10.1039/d3ra04953a  
[rsc.li/rsc-advances](http://rsc.li/rsc-advances)

# Ionic liquid immobilized on modified magnetic FSM-16: an efficient and magnetically recoverable nanocatalyst†

 Azar Jahanbakhshi and Mahnaz Farahi \*

In the present article, a nanocomposite was prepared by immobilizing ionic liquid on the magnetic mesoporous FSM-16 with a core–shell structure ( $\text{Fe}_3\text{O}_4@\text{FSM-16-SO}_3/\text{IL}$ ). Subsequently, the structural properties of the synthesized nanocatalyst were characterized and analyzed by various techniques such as XRD, FT-IR, TEM, FE-SEM, BET, VSM, TGA, and EDS.  $\text{Fe}_3\text{O}_4@\text{FSM-16-SO}_3/\text{IL}$  was used as a recoverable and efficient nanocatalyst for the synthesis of polyhydroquinoline derivatives. The magnetic nanocatalyst showed remarkable stability and reusability and was reused six consecutive times without considerable loss of its activity.

## 1. Introduction

In recent years, various types of mesoporous materials with high surface area, high pore volume, and large pore size have been synthesized using different surfactant templating procedures to expand their applications in the field of heterogeneous catalysts.<sup>1,2</sup> Among the different mesoporous materials with structure and very regular pores, MCM-41 and FSM-16 have attracted much attention due to their many applications in various fields such as drug delivery, chromatography, adsorbents, electrodes, and also catalysts.<sup>3–8</sup> FSM-16 structures have been prepared by intercalation of quarterly ammonium surfactant as a template into layered sodium silicate, kanemite, followed by calcination to remove the template, resulting in the formation of a hexagonal arrangement of channels with active surface silanol groups, high surface area, and uniform pore size.<sup>9–11</sup> Some important studies reported on the FSM-16 based nanocatalysts are  $\text{FSM-16}@$ imine-thiophen/Pd,<sup>12</sup>  $\text{Fe}_3\text{O}_4@\text{FSM-16-SO}_3\text{H}$ ,<sup>13</sup>  $\text{FSM-16-Met}$ ,<sup>14</sup>  $\text{FSM-16-SO}_3\text{H}$ ,<sup>15</sup> and  $\text{FSM-16/AEPC-SO}_3\text{H}$ .<sup>16</sup> Although porous nanomaterials have been widely used as supports for the preparation of heterogeneous catalysts, one of the major problems of them is the difficulty of separation from the reaction mixture by filtration and centrifugation. The key to overcoming these limitations is the use of magnetic nanoparticles (MNPs), which allow easy and faster separation of the porous nanomaterials from the reaction mixture by an external magnetic field.<sup>17–19</sup> The combination of the properties of magnetic nanoparticles and mesoporous materials in a single material is particularly attractive from the point of view

of catalysis because of possibility of combining the various functional groups with the advantages of the magnetic properties of magnetic nanoparticles. Therefore, magnetic mesoporous materials have attracted considerable attention as an attractive support for heterogeneous catalysts due to their superior properties such as environmentally benign nature, high stability, uniform porosity, easy separation, and recycling by applying a permanent magnet.<sup>20–22</sup>

New and innovative research in the field of green chemistry extensively discusses waste and damage reduction, innate atom economy, energy conservation, ease of use and the avoidance of perilous chemicals. Another important aspect of green chemistry is the use of ionic liquids (ILs) as new, green, and environmentally friendly solvents compared to toxic solvents for synthetic chemistry. In addition, ILs have attracted a wide application in the field of catalysis chemistry due to their unique properties such as high ionic conductivity, non-flammability, tunable acidity and basicity, high selectivity, high thermal stability, and reusability, and have been used in many organic reactions.<sup>23–26</sup> The zwitterionic salts (ZIs) are organic salts that are composed of covalently bonded cations and anions. Zwitterions do not dissociate into ions, thus avoiding unwanted partitioning of ions can be avoided. The intramolecular covalent bonding of the cationic and anionic sites of zwitterions makes them stronger hydrogen bond donors or acceptors than their ionic liquid counterparts.<sup>19,27,28</sup> Another interesting feature of ZIs is their ability to act as precursors for Brønsted acidic ionic liquids, which are widely used as solvents and catalysts in various organic reactions. However, the problems of recyclability and high viscosity have limited the use of ionic liquids use in catalytic reactions. A combination of interesting properties of the ionic liquid with those of the support material will develop novel performances when synergistic effects occur. Therefore, immobilization of ionic liquids on

Department of Chemistry, Yasouj University, Yasouj, 75918-74831, Iran. E-mail: [farahim@yu.ac.ir](mailto:farahim@yu.ac.ir); Fax: +98-7412242167

† Electronic supplementary information (ESI) available. See DOI: <https://doi.org/10.1039/d3ra04953a>



suitable solid supports such as porous supports or magnetic nanoparticles would be a short cut to achieve better catalytic efficiency and recycling performance than current ionic liquid catalysts.<sup>29–33</sup> To date, many ionic liquids supported on magnetic mesoporous materials have been prepared and used in many chemical reactions. Some of the recently developed systems are  $\text{Fe}_3\text{O}_4$ @silica-MCM-41@DABCO,<sup>34</sup>  $\text{Fe}_3\text{O}_4$ @MCM-41@IL/Pd,<sup>35</sup> MCM-41@ILLaCl<sub>4</sub>,<sup>36</sup> I@BFPMO-IL,<sup>37</sup>  $\text{Fe}_3\text{O}_4$ @MCM-41@ZrCl<sub>2</sub>,<sup>38</sup>  $\text{Fe}_3\text{O}_4$ @MCM-41-SO<sub>3</sub>H@[HMIm]  
[HSO<sub>4</sub>]<sup>39</sup>  $\text{Fe}_3\text{O}_4$ @MCM@IL-WO<sub>4</sub><sup>40</sup> SBA-15/NHSO<sub>3</sub>H,<sup>41</sup> and  $\text{Fe}_3\text{O}_4$ @SiO<sub>2</sub>-HMTA-SO<sub>3</sub>H.<sup>42</sup> The heterogenization of IL catalysts can also be achieved by the construction of poly(ionic liquid)s, and several catalysts of this type have been reported.<sup>43–45</sup>

Nitrogen-containing heterocycles often play an important role as the scaffolds for pharmacological compounds. Polyhydroquinoline derivatives, as an important class of N-heterocyclic compounds have become an important structural component in many pharmaceutical agents such as HIV protease inhibition, antitumor, neurotropic, antibacterial, MDR reversal, antimutagenic, antidiabetic, hepatoprotective, and vasodilator.<sup>46–48</sup> Therefore, considering the medicinal and biological significance, the synthesis of this class of heterocyclic compounds has attracted considerable attention from synthetic chemists. Polyhydroquinoline derivatives are usually synthesized *via* the four-compound one-pot reaction of aldehyde, dimedone, ethyl acetoacetate, ammonium acetate, and the corresponding catalyst.<sup>49–51</sup>

In continuation of our studies program for the synthesis of novel heterogeneous nanocatalysts and also considering the importance of mesoporous materials in the catalysis synthesis process,<sup>12,52–58</sup> herein, a recyclable magnetic catalyst based on FSM-16 ( $\text{Fe}_3\text{O}_4$ @FSM-16-SO<sub>3</sub>/IL) has been synthesized and characterized. Furthermore,  $\text{Fe}_3\text{O}_4$ @FSM-16-SO<sub>3</sub>/IL was used as an effective catalyst in the synthesis of polyhydroquinoline derivatives *via* the one-pot reaction of various aromatic aldehydes, dimedone, ethyl acetoacetate, and ammonium acetate.

## 2. Experimental

### 2.1. General

All solvents, chemicals, and reagents were purchased from Fluka, Merck, and Sigma-Aldrich companies. The purchased materials including  $\text{FeCl}_3 \cdot 6\text{H}_2\text{O}$ ,  $\text{FeCl}_2 \cdot 4\text{H}_2\text{O}$ , sodium hydroxide (NaOH), cetyltrimethyl ammonium bromide (CTAB), tetraethyl *ortho* silicate (TEOS), cholorosulfonic acid (ClSO<sub>3</sub>H), triethyl amine (TEA), 1,4-butane sultone, dimedone, ethyl acetoacetate, ammonium acetate, benzaldehyde, 4-nitrobenzaldehyde, 4-chlorobenzaldehyde, 4-methylbenzaldehyde, 3-methoxybenzaldehyde, 3-bromobenzaldehyde, 2-chlorobenzaldehyde, 2,4-chlorobenzaldehyde, 2-hydroxy-3-methoxybenzaldehyde, ethanol, toluene, 1,4-dioxane, and dichloromethane, and were used without further purification. X-ray diffraction (XRD) analysis was investigated using a Rigaku Ultima IV diffractometer. Field emission-scanning electron microscopy (FE-SEM) images were recorded using FE-SEM TESCAN MIRA3. The energy-dispersive X-ray (EDX) spectrum

was measured using a TESCAN VEGA model. Thermo gravimetric (TGA) analysis was performed using a PerkinElmer STA 6000 instrument. Transmission electron microscopy (TEM) images were examined using Philips EM208S instrument. The surface area was evaluated using the Brunauer–Emmett–Teller (BET) technique. The magnetic properties of the materials were monitored using a vibrating sample magnetometer (VSM) model MDK VSM. The FT-IR spectra in the range of 400–4000 cm<sup>−1</sup> were obtained using FT-IR JASCO-Model 680 spectroscopy. The NMR spectroscopy was performed on a Bruker 400 MHz Ultrashield instrument at 400 MHz (<sup>1</sup>H-NMR) and 100 MHz (<sup>13</sup>C-NMR) in DMSO-*d*<sub>6</sub> as solvent.

### 2.2. Synthesis of $\text{Fe}_3\text{O}_4$ nanoparticles

Initially,  $\text{Fe}_3\text{O}_4$  NPs were prepared by adding  $\text{FeCl}_3 \cdot 6\text{H}_2\text{O}$  (2.7 g, 10 mmol) and  $\text{FeCl}_2 \cdot 4\text{H}_2\text{O}$  (1 g, 5 mmol) to deionized water (50 mL), followed by a dropwise addition of sodium hydroxide solution (5 mL, 10 M) with stirring at 80 °C under an N<sub>2</sub> atmosphere for 1 h. The magnetic precipitate was then collected with a magnet and washed through deionized water and ethanol. The precipitate obtained was dried in an oven at 70 °C for 2 h.<sup>54</sup>

### 2.3. Synthesis of $\text{Fe}_3\text{O}_4$ @FSM-16

Sodium hydroxide (3 g) was dissolved in deionized water (30 mL). Tetraethyl *ortho* silicate (TEOS) (16.6 mL) was added dropwise to the NaOH solution over 1 h and the resulting mixture was stirred for 24 h at 80 °C. The mixture was centrifuged and washed with deionized water, and dried at 80 °C for 12 h. The resulting product was then calcined in an oven at 650 °C for 5 h, and finally, the product of kanemite ( $\delta$ -Na<sub>2</sub>Si<sub>2</sub>O<sub>5</sub>) was synthesized. Kanemite (5 g) was added to deionized water (50 mL) and stirred at 30 °C for 3 h. The resulting suspension was then filtered to obtain the wet kanemite dough. Next,  $\text{Fe}_3\text{O}_4$  nanoparticles (0.106 g, 0.457 mmol) were dispersed in deionized water (50 mL) by ultrasonic waves and cetyltrimethylammonium bromide (CTAB) was added to this solution by slowly raising the temperature to 70 °C. Then, the kanemite paste was added and then stirred at 70 °C for 3 h. At this stage, the pH value of the suspension was 11.5–12.5. After 3 h, the pH of the medium was adjusted to 8.5 with HCl (2 M), and the mixture was stirred at 70 °C for another 3 h. After cooling the mixture, the resulting solid was separated by centrifugation and washed with deionized water. The magnetite mesoporous silicate ( $\text{Fe}_3\text{O}_4$ @FSM-16) was dried in an oven at 80 °C for 2 h and then calcined in an oven at 650 °C for 5 h to burn the surfactant and synthesis of the final magnetite mesoporous silicate,  $\text{Fe}_3\text{O}_4$ @FSM-16.<sup>13</sup>

### 2.4. Synthesis of $\text{Fe}_3\text{O}_4$ @FSM-16-SO<sub>3</sub>H

$\text{Fe}_3\text{O}_4$ @FSM-16 (0.5 g) was then sonicated for 15 min in dry  $\text{CH}_2\text{Cl}_2$  (5 mL) in a 10 mL round bottom flask. Then cholorosulfonic acid (ClSO<sub>3</sub>H) (0.15 mL) was added dropwise to the reaction mixture for 15 min at room temperature. The reaction mixture was stirred for 2 h. Finally, the brown solid was



separated with an external magnet and was dried in an oven at 100 °C for 2 h to obtain  $\text{Fe}_3\text{O}_4@\text{FSM-16-SO}_3\text{H}$ .<sup>13</sup>

### 2.5. Preparation of zwitterionic salts $[(\text{CH}_2)_4\text{SO}_3\text{TEA}]$

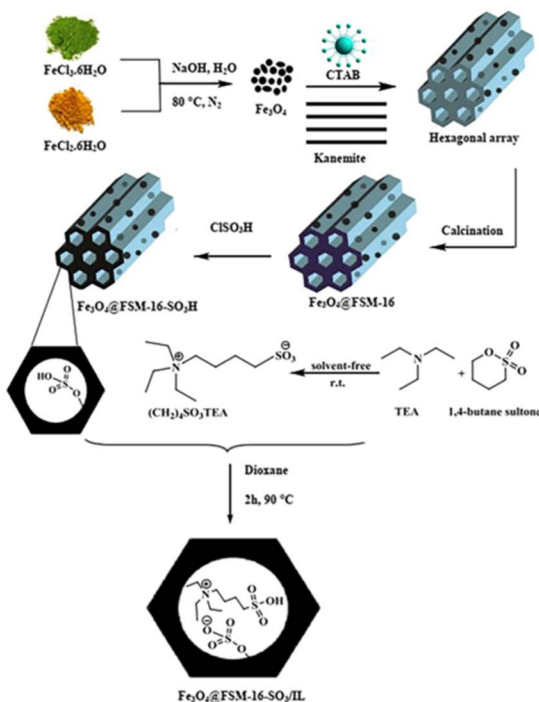
The zwitterionic solid was synthesized by a one-step reaction between triethylamine (1 mmol) and 1,4-butane sultone (1 mmol) under solvent-free conditions and stirring at room temperature for 24 h. The resulting solid salt was washed several times with diethyl ether and dried in a vacuum at 60 °C.<sup>59</sup>

### 2.6. Electrostatic immobilization of ionic liquid on $\text{Fe}_3\text{O}_4@\text{FSM-16-SO}_3\text{H}$ [ $\text{Fe}_3\text{O}_4@\text{FSM-16-SO}_3/\text{IL}$ ]

Ultimately,  $\text{Fe}_3\text{O}_4@\text{FSM-16-SO}_3\text{H}$  groups (1 g) in toluene (20 mL) were dispersed by sonication for 15 min and  $[(\text{CH}_2)_4\text{SO}_3\text{TEA}]$  (0.6 g) in 1,4-dioxane (15 mL) was added to the mixture at room temperature. The temperature of the reaction was then slowly increased to 85 °C and stirred for 3 h. The reaction solvent was removed under a vacuum at 85 °C. The  $\text{Fe}_3\text{O}_4@\text{FSM-16-SO}_3/\text{IL}$  catalyst obtained was washed with ethanol and dried under vacuum at 65 °C.

### 2.7. General procedure for the synthesis of polyhydroquinoline derivatives using $\text{Fe}_3\text{O}_4@\text{FSM-16-SO}_3/\text{IL}$ nanocatalyst

A mixture of aldehyde (1 mmol), dimedone (1 mmol), ethyl acetoacetate (1 mmol), ammonium acetate (1.2 mmol), and  $\text{Fe}_3\text{O}_4@\text{FSM-16-SO}_3/\text{IL}$  nanocatalyst (0.004 g) in ethanol (5 mL)



**Scheme 1** Functionalization of FSM-16 and electrostatic immobilization of IL.

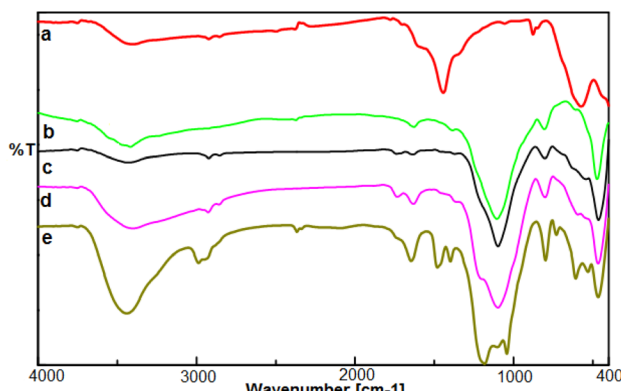


**Fig. 1** The FT-IR spectrum of (a)  $\text{Fe}_3\text{O}_4$ , (b) FSM-16, (c)  $\text{Fe}_3\text{O}_4@\text{FSM-16}$ , (d)  $\text{Fe}_3\text{O}_4@\text{FSM-16-SO}_3\text{H}$ , and (e)  $\text{Fe}_3\text{O}_4@\text{FSM-16-SO}_3/\text{IL}$ .

was stirred under reflux conditions. The progress of the reaction was monitored by TLC (*n*-hexane/ethyl acetate, 2 : 1).

At the end of the reaction, the  $\text{Fe}_3\text{O}_4@\text{FSM-16-SO}_3/\text{IL}$  nanocatalyst was separated by an external magnet. Finally, the pure products were purified by recrystallization from MeOH.

### 2.8. Recovery

$\text{Fe}_3\text{O}_4@\text{FSM-16-SO}_3/\text{IL}$  (0.004 g) was added to the mixture of aldehyde (1 mmol), dimedone (1 mmol), ethyl acetoacetate (1 mmol) and ammonium acetate (1.2 mmol) in (5 mL) ethanol and stirred under reflux conditions. After completion of the reaction, hot methanol (10 mL) was added to the reaction mixture; the catalyst was separated by an external magnet, washed three times with MeOH, and dried. The isolated catalyst was used directly for the subsequent runs under similar conditions.

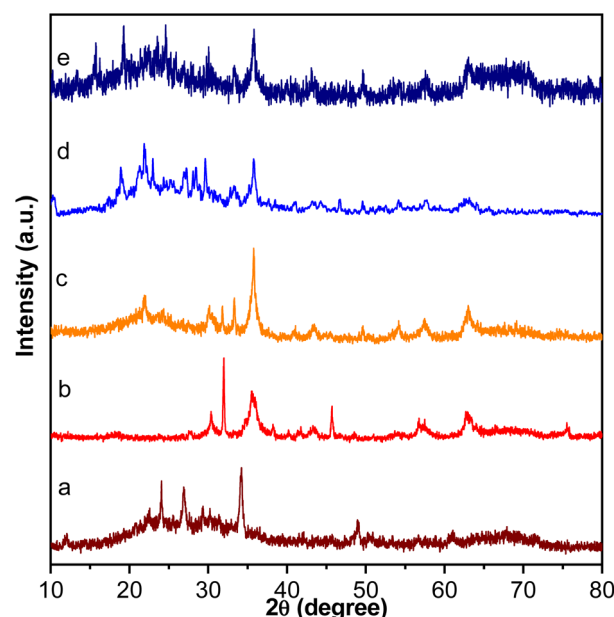


**Fig. 2** XRD patterns of (a) FSM-16, (b)  $\text{Fe}_3\text{O}_4$ , (c)  $\text{Fe}_3\text{O}_4@\text{FSM-16}$ , (d)  $\text{Fe}_3\text{O}_4@\text{FSM-16-SO}_3\text{H}$ , and (e)  $\text{Fe}_3\text{O}_4@\text{FSM-16-SO}_3/\text{IL}$ .



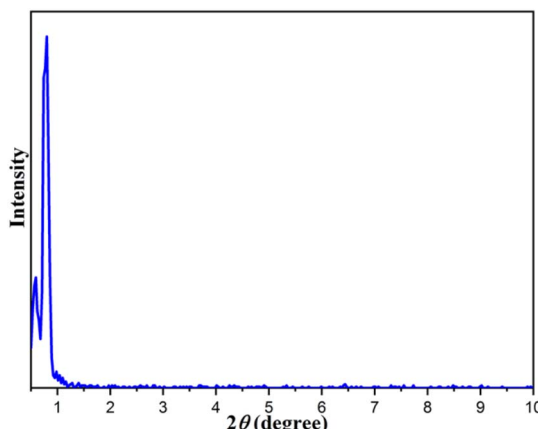


Fig. 3 XRD low angle XRD patterns of  $\text{Fe}_3\text{O}_4@\text{FSM-16-SO}_3/\text{IL}$ .

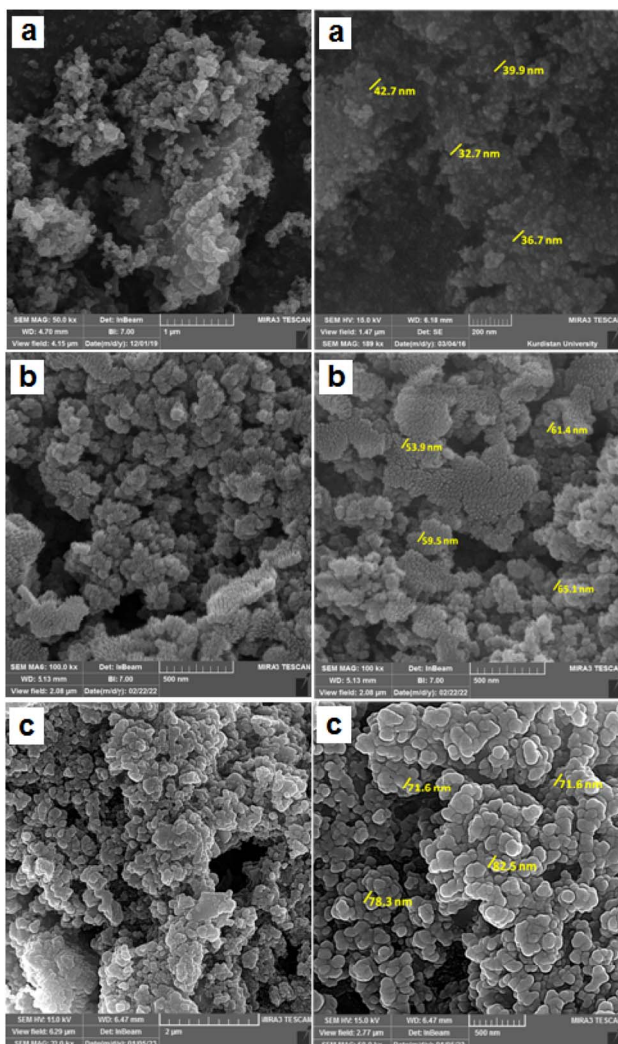


Fig. 4 The FE-SEM images of (a)  $\text{Fe}_3\text{O}_4$ , (b) FSM-16 (image (b) has been reused from a previous publication, <https://doi.org/10.1039/D2RA06271B>),<sup>12</sup> and (c)  $\text{Fe}_3\text{O}_4@\text{FSM-16-SO}_3/\text{IL}$ .

### 3. Results and discussion

#### 3.1. Synthesis and characterization of the catalyst

In this work, for the preparation of  $\text{Fe}_3\text{O}_4@\text{FSM-16-SO}_3/\text{IL}$ , the acidic ionic liquid immobilization on  $\text{Fe}_3\text{O}_4@\text{FSM-16}$  nanocomposite was performed in several steps as shown in Scheme 1. Firstly,  $\text{Fe}_3\text{O}_4$  nanoparticles were prepared and then coated with CTAB and kanemite ( $\delta\text{-Na}_2\text{Si}_2\text{O}_5$ ). The resulting product was calcined to produce  $\text{Fe}_3\text{O}_4@\text{FSM-16}$ . Subsequently,  $\text{Fe}_3\text{O}_4@\text{FSM-16-SO}_3\text{H}$  was prepared by the reaction of between  $\text{Fe}_3\text{O}_4@\text{FSM-16}$  with chlorosulfonic acid. Then, the reaction of triethylamine with 1,4-butane sultone produced the ionic liquid (IL). Finally, the  $\text{Fe}_3\text{O}_4@\text{FSM-16-SO}_3/\text{IL}$  nanocatalyst was prepared by the electrostatic stabilization the IL on  $\text{Fe}_3\text{O}_4@\text{FSM-16-SO}_3\text{H}$ . The synthesized nanocatalyst was characterized by XRD, FT-IR, TGA, FE-SEM, EDS, TEM, BET, and VSM analyses.

The FT-IR spectra of  $\text{Fe}_3\text{O}_4$ , FSM-16,  $\text{Fe}_3\text{O}_4@\text{FSM-16}$ ,  $\text{Fe}_3\text{O}_4@\text{FSM-16-SO}_3\text{H}$ , and  $\text{Fe}_3\text{O}_4@\text{FSM-16-SO}_3/\text{IL}$  were compared to analyze the progress of the catalyst synthesis (Fig. 1). In Fig. 1a, the absorption bands revealed at 574 and  $3400\text{ cm}^{-1}$  are attributed to Fe–O and O–H bonds, respectively.<sup>54,56</sup> Also, in Fig. 1b, the peaks at 474, 806, and  $1106\text{ cm}^{-1}$  correspond to asymmetric and symmetric stretching vibrations of the Si–O–Si group.<sup>12</sup> In Fig. 1c, the peaks of the Fe–O bond at  $588\text{ cm}^{-1}$  overlap with the S–O bond at about  $600\text{ cm}^{-1}$ . The increase in

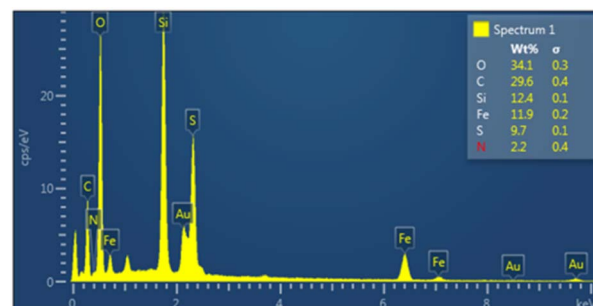


Fig. 5 The EDX spectra of  $\text{Fe}_3\text{O}_4@\text{FSM-16-SO}_3/\text{IL}$ .

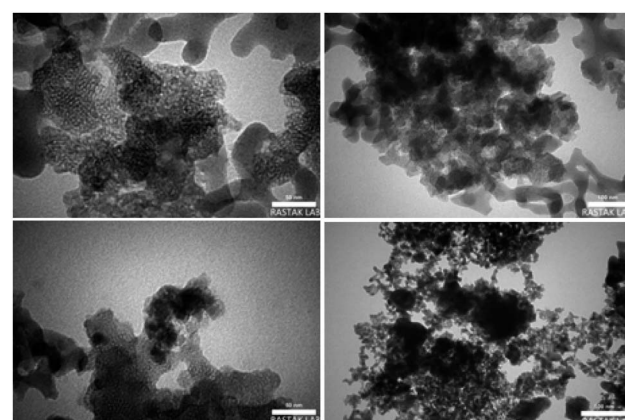


Fig. 6 TEM images of  $\text{Fe}_3\text{O}_4@\text{FSM-16-SO}_3/\text{IL}$ .



the intensity of the peak at  $1106\text{ cm}^{-1}$  is related to the  $\text{O}=\text{S}=\text{O}$  band, indicating the  $-\text{SO}_3\text{H}$  group in the  $\text{Fe}_3\text{O}_4@\text{FSM-16-SO}_3\text{H}$  (Fig. 1d).<sup>39,41</sup> The stretching band at about  $2950\text{ cm}^{-1}$  corresponds to the  $\text{CH}_2$  groups, and the appearing bands at  $1400\text{--}1600\text{ cm}^{-1}$  are related to the stretching vibrations of  $\text{C}-\text{C}$  and  $\text{C}-\text{N}$  (Fig. 1e).<sup>4,59</sup>

The XRD patterns of the FSM-16,  $\text{Fe}_3\text{O}_4$ ,  $\text{Fe}_3\text{O}_4@\text{FSM-16}$ ,  $\text{Fe}_3\text{O}_4@\text{FSM-16-SO}_3\text{H}$ , and  $\text{Fe}_3\text{O}_4@\text{FSM-16-SO}_3/\text{IL}$  in the range of  $2\theta = 10\text{--}80^\circ$  are shown in Fig. 2. In Fig. 2a, the four characteristic peaks at  $2\theta = 23.4^\circ$ ,  $37.1^\circ$ ,  $48.5^\circ$  and  $61.5^\circ$  related to the  $(100)$ ,  $(110)$ ,  $(200)$ , and  $(210)$  planes of FSM-16 with regular hexagonal structures.<sup>8,11,12</sup> In the XRD pattern of  $\text{Fe}_3\text{O}_4$  nanoparticles, six peaks indicated at  $2\theta = 30.26^\circ$ ,  $35.7^\circ$ ,  $43.5^\circ$ ,  $53.59^\circ$ ,  $57.5^\circ$ , and  $63.26^\circ$  related to the  $(2\ 2\ 0)$ ,  $(3\ 1\ 1)$ ,  $(4\ 0\ 0)$ ,  $(4\ 2\ 2)$ ,  $(5\ 1\ 1)$ , and  $(4\ 4\ 0)$  which confirm the spinel structure of  $\text{Fe}_3\text{O}_4$  (Fig. 2b).<sup>54,56,57</sup> As shown in Fig. 2c, the XRD pattern of  $\text{Fe}_3\text{O}_4@\text{FSM-16}$  is in good agreement with the XRD pattern of previous reports of  $\text{Fe}_3\text{O}_4$  coated FSM-16 structures ( $\text{Fe}_3\text{O}_4@\text{FSM-16}$ ).<sup>13</sup> Furthermore, as shown in Fig. 2d, the peak intensities are slightly reduced, which is due to the stabilization of  $-\text{SO}_3\text{H}$  acidic groups on the surface  $\text{Fe}_3\text{O}_4@\text{FSM-16}$ . According to Fig. 2e, the XRD pattern of the  $\text{Fe}_3\text{O}_4@\text{FSM-16-SO}_3/\text{IL}$  nanocatalyst has been changed due to the immobilization of IL on

$\text{Fe}_3\text{O}_4@\text{FSM-16-SO}_3\text{H}$ . Also, the comparison of Fig. 2e with Fig. 2b and c confirms the immobilization of  $\text{Fe}_3\text{O}_4$ ,  $-\text{SO}_3\text{H}$ , and IL on FSM-16, and shows that the  $\text{Fe}_3\text{O}_4@\text{FSM-16-SO}_3/\text{IL}$  catalyst was successfully synthesized.

In addition, the low angle X-ray diffraction (LXRD) analysis of the  $\text{Fe}_3\text{O}_4@\text{FSM-16-SO}_3/\text{IL}$  catalyst in Fig. 3 shows a high intensity peak at  $2\theta = 0.91^\circ$  corresponding to  $(1\ 0\ 0)$ , which is characteristic of hexagonally ordered mesoporous materials.

The surface morphology, particle size and structural features of  $\text{Fe}_3\text{O}_4$ , FSM-16,<sup>12</sup> and  $\text{Fe}_3\text{O}_4@\text{FSM-16-SO}_3/\text{IL}$  nanocatalyst were identified by using field effect scanning electron microscopy (FE-SEM) (Fig. 4). The FE-SEM images show that the synthesized nanocatalyst has an almost regular spherical morphology and uniformity and is less than 100 nm in particle size. Furthermore, it is obvious from Fig. 4 that the average

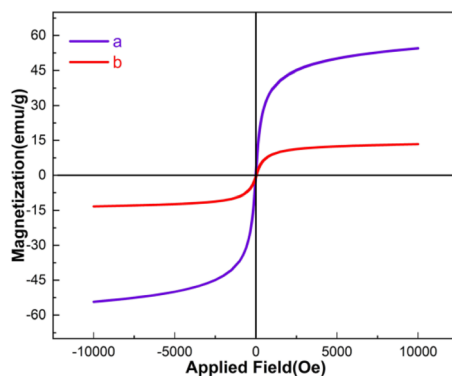


Fig. 7 VSM curves of the (a)  $\text{Fe}_3\text{O}_4$  and (b)  $\text{Fe}_3\text{O}_4@\text{FSM-16-SO}_3/\text{IL}$ .

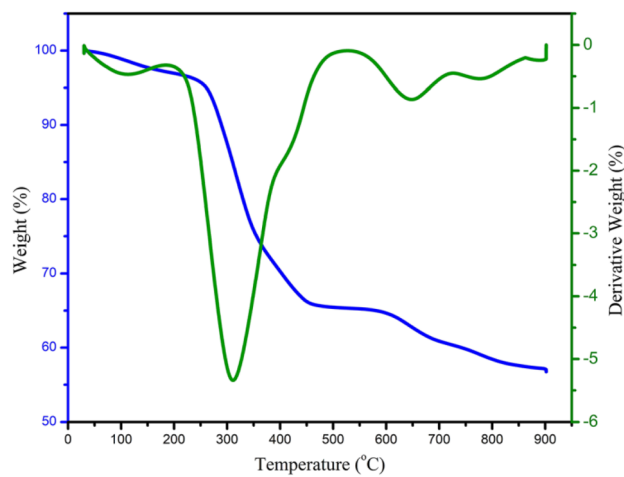


Fig. 8 TGA analysis of the  $\text{Fe}_3\text{O}_4@\text{FSM-16-SO}_3/\text{IL}$ .

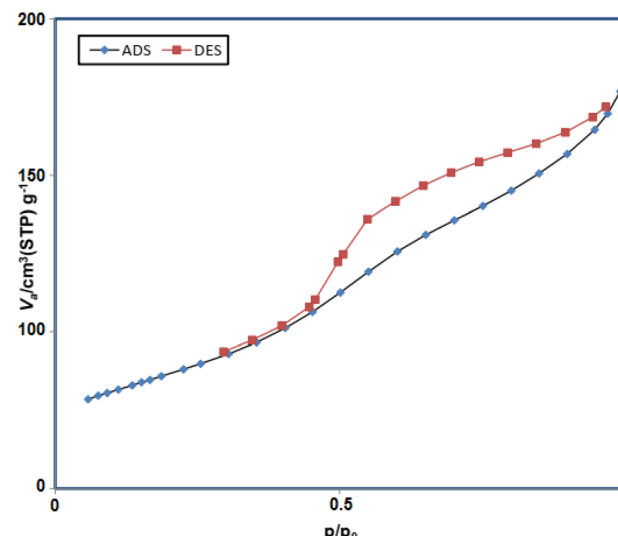
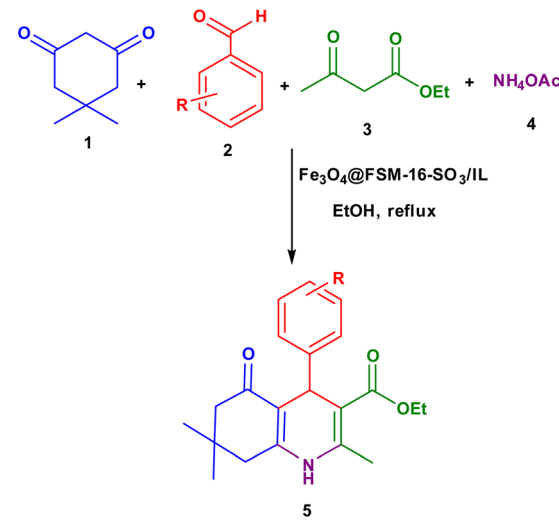


Fig. 9  $\text{N}_2$  adsorption–desorption isotherms of  $\text{Fe}_3\text{O}_4@\text{FSM-16-SO}_3/\text{IL}$ .



Scheme 2 Synthesis of polyhydroquinoline derivatives 5 using  $\text{Fe}_3\text{O}_4@\text{FSM-16-SO}_3/\text{IL}$  nanocatalyst.



**Table 1** Optimization of the reaction conditions for the synthesis of 5a<sup>a</sup>

Entry	Catalyst loading (g)	Solvent	Temp. (°C)	Yield <sup>b</sup> (%)
1	0.002	—	80	55
2	0.004	—	80	94
3	0.005	—	80	94
4	0.007	—	80	94
5	0.004	EtOH	Reflux	96
6	0.004	H <sub>2</sub> O	80	65
7	0.004	CH <sub>3</sub> CN	80	55
8	0.004	DMSO	80	60
9	0.004	Toluene	80	45
10	0.004	EtOH	25	40
11	0.004	EtOH	50	60

<sup>a</sup> Reaction conditions: benzaldehyde (1 mmol), dimedone (1 mmol), ethyl acetoacetate (1 mmol), ammonium acetate (1.2 mmol). Time: 30 min. <sup>b</sup> Isolated yields.

particle size of Fe<sub>3</sub>O<sub>4</sub> and FSM-16 significantly changed after stabilization with SO<sub>3</sub>H and IL, which indicates the successful synthesis of Fe<sub>3</sub>O<sub>4</sub>@FSM-16-SO<sub>3</sub>/IL.

As shown in Fig. 5, energy-dispersive X-ray (EDX) analysis was used to determine the elements of nanoporous Fe<sub>3</sub>O<sub>4</sub>@FSM-16-SO<sub>3</sub>/IL. The results confirm the presence of C, O, N, S,

Si, and Fe in the synthesized nanocatalyst, and it could be inferred that the target catalyst was successfully synthesized.

The TEM images of Fe<sub>3</sub>O<sub>4</sub>@FSM-16-SO<sub>3</sub>/IL catalyst are shown in Fig. 6. As seen in the images, the black cores of Fe<sub>3</sub>O<sub>4</sub> NPs are surrounded by a grey shell of FSM-16-SO<sub>3</sub>/IL.

The magnetic properties of the Fe<sub>3</sub>O<sub>4</sub> and Fe<sub>3</sub>O<sub>4</sub>@FSM-16-SO<sub>3</sub>/IL were investigated using the vibrating sample magnetometer (VSM) technique at room temperature (Fig. 7). Based on the VSM curves, the magnetization was measured to be Fe<sub>3</sub>O<sub>4</sub> 53.03 emu g<sup>-1</sup>, and for Fe<sub>3</sub>O<sub>4</sub>@FSM-16-SO<sub>3</sub>/IL 15.5 emu per g nanocatalyst. It is essential to notice that the decrease in the magnetization value Fe<sub>3</sub>O<sub>4</sub>@FSM-16-SO<sub>3</sub>/IL nanocatalyst compared to Fe<sub>3</sub>O<sub>4</sub> may be due to the immobilization of the shell of FSM-16-SO<sub>3</sub>H and then IL around the magnetic Fe<sub>3</sub>O<sub>4</sub> cores. The results showed that even with the reduction of the magnetization; the catalyst can be successfully separated from the reaction mixture by an external magnet.

To investigate the thermal stability of the Fe<sub>3</sub>O<sub>4</sub>@FSM-16-SO<sub>3</sub>/IL nanocatalyst, the thermo gravimetric analysis (TGA) was performed in the range of 25–900 °C (Fig. 8). Based on the TGA spectrum, the first weight loss of about 4.6% at a temperature below 220 °C was related to the removal of water, physically and chemically absorbed solvents, and surface hydroxyl groups on the Fe<sub>3</sub>O<sub>4</sub>@FSM-16-SO<sub>3</sub>/IL surface. The second and largest weight loss in the range of 220–480 °C is about 28%, related to the thermal decomposition of the sulfuric acid group, amine

**Table 2** Synthesis of derivatives 5 using Fe<sub>3</sub>O<sub>4</sub>@FSM-16-SO<sub>3</sub>/IL nanocatalyst<sup>a</sup>

Entry	Aldehyde	Product 5	M. p. (°C)	Yield <sup>b</sup> (%)
5a	C <sub>6</sub> H <sub>5</sub> CHO		204–206 (ref. 65)	98
5b	4-OMe-C <sub>6</sub> H <sub>4</sub> CHO		252–254 (ref. 65)	92
5c	4-NO <sub>2</sub> -C <sub>6</sub> H <sub>4</sub> CHO		236–238 (ref. 65)	93



Table 2 (Contd.)

Entry	Aldehyde	Product 5	M. p. (°C)	Yield <sup>b</sup> (%)
5d	4-Cl-C <sub>6</sub> H <sub>4</sub> CHO		243–244 (ref. 60)	92
5e	2-Cl-C <sub>6</sub> H <sub>4</sub> CHO		208–210 (ref. 60)	95
5f	2,4-Cl <sub>2</sub> -C <sub>6</sub> H <sub>3</sub> CHO		244–245 (ref. 62)	96
5g	3-Br-C <sub>6</sub> H <sub>4</sub> CHO		234–236 (ref. 62)	92
5h	4-Me-C <sub>6</sub> H <sub>4</sub> CHO		270–272 (ref. 62)	93
5i	2-OH-3-OMe-C <sub>6</sub> H <sub>3</sub> CHO		210–212 (ref. 63)	92

<sup>a</sup> Reaction conditions: aromatic aldehyde (1 mmol), dimedone (1 mmol), ethyl acetoacetate (1 mmol), ammonium acetate (1.2 mmol), Fe<sub>3</sub>O<sub>4</sub>@FSM-16-SO<sub>3</sub>/IL (0.004 g), EtOH (5 mL), reflux conditions. Time: 5–20 min. <sup>b</sup> Isolated yields.

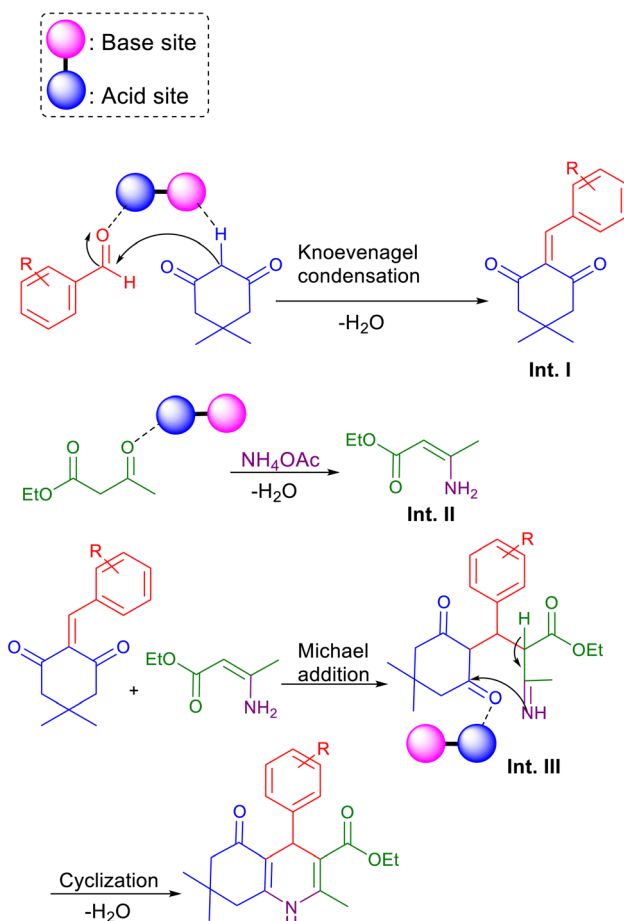


group, and organic groups on the surface of the  $\text{Fe}_3\text{O}_4@\text{FSM-16}$  nanocomposite. The third and last weight loss of about 8% between 480 and 900  $^{\circ}\text{C}$  is related to the thermal complete decomposition of  $\text{Fe}_3\text{O}_4@\text{FSM-16}$  and the ionic liquid (IL) stabilized on its surface, confirming the thermal stability of the prepared  $\text{Fe}_3\text{O}_4@\text{FSM-16-SO}_3/\text{IL}$  nanocatalyst.

In addition, based on the physicochemical and structural parameters of  $\text{Fe}_3\text{O}_4@\text{FSM-16-SO}_3/\text{IL}$  nanocatalyst, the nitrogen adsorption–desorption isotherms were measured (Fig. 9). The type of  $\text{N}_2$  adsorption–desorption isotherm of prepared nanocatalyst, according to the IUPAC classification, is a type III isotherm, which indicating of the typical mesoporous structure. Furthermore, according to the Brunauer–Emmett–Teller (BET) analysis, the surface area, total pore volume, and mean pore diameter of the  $\text{Fe}_3\text{O}_4@\text{FSM-16-SO}_3/\text{IL}$  catalyst  $180 \text{ m}^2 \text{ g}^{-1}$ ,  $0.02 \text{ cm}^3 \text{ g}^{-1}$ , and  $5.83 \text{ nm}$  were obtained respectively.

### 3.2. Synthesis of polyhydroquinoline derivatives

After the successful characterization of the  $\text{Fe}_3\text{O}_4@\text{FSM-16-SO}_3/\text{IL}$  nanocatalyst, its catalytic application was investigated in the synthesis of polyhydroquinoline derivatives with the multi-component reaction of aromatic aldehyde, dimedone, ethyl acetoacetate, and ammonium acetate (Scheme 2).



Scheme 3 The suggested mechanism for the synthesis of polyhydroquinoline derivatives 5 using  $\text{Fe}_3\text{O}_4@\text{FSM-16-SO}_3/\text{IL}$ .

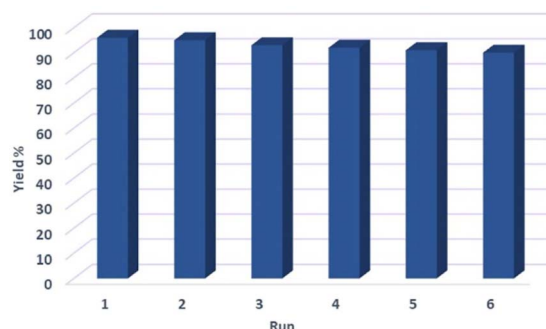


Fig. 10 Reusability of  $\text{Fe}_3\text{O}_4@\text{FSM-16-SO}_3/\text{IL}$  in the synthesis of 5a.

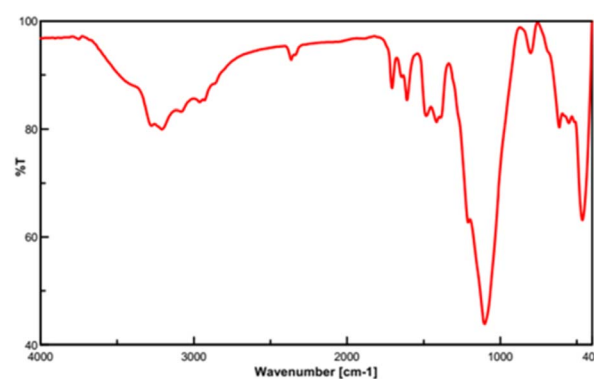


Fig. 11 FT-IR spectrum of the recycled  $\text{Fe}_3\text{O}_4@\text{FSM-16-SO}_3/\text{IL}$  catalyst.

Initially, to obtain the best reaction conditions, a one-pot reaction between benzaldehyde, dimedone, ethyl acetoacetate, and ammonium acetate as a model reaction was investigated. For this purpose, the effect of catalyst loading, temperature, and solvent was studied. Primarily, the catalytic efficiency of the  $\text{Fe}_3\text{O}_4@\text{FSM-16-SO}_3/\text{IL}$  nanocatalyst was investigated. The catalyst loading study showed that the use of 0.004 g of  $\text{Fe}_3\text{O}_4@\text{FSM-16-SO}_3/\text{IL}$  gave the highest conversion. Then, to obtain the optimum solvent, the model reaction was carried out in

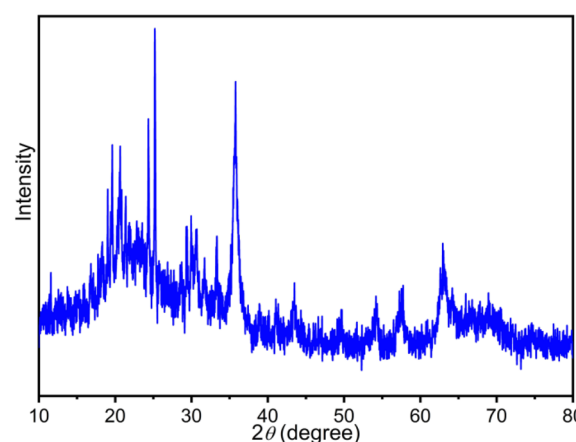


Fig. 12 XRD pattern of the recycled  $\text{Fe}_3\text{O}_4@\text{FSM-16-SO}_3/\text{IL}$  catalyst.



**Table 3** Comparison results of  $\text{Fe}_3\text{O}_4@\text{FSM-16-SO}_3/\text{IL}$  with other catalysts for the synthesis of polyhydroquinoline derivatives

Catalyst	Conditions	Time (min)	Yield <sup>a</sup> (%)
$\text{Fe}_3\text{O}_4@\text{SiO}_2/\text{ZnCl}_2$	Cat. (0.05), solvent-free, 110 °C	25	94 (ref. 61)
SPPN	Cat. (6 mg), EtOH, MW	8	96 (ref. 62)
TrzMOP	Cat. (8 mg), EtOH, 120 °C, MW	10	98 (ref. 63)
$[\text{TBA}]_2[\text{W}_6\text{O}_{19}]$	Cat. (0.07 mmol), solvent-free, 110 °C	20	93 (ref. 64)
GSA@MNPs	Cat. (0.05 mg), EtOH, reflux	240	90 (ref. 65)
$\text{H}_2\text{SO}_4$	Cat. (0.004 g), EtOH, reflux	720	— <sup>b</sup>
$\text{Fe}_3\text{O}_4@\text{FSM-16-SO}_3/\text{IL}$	Cat. (0.004 g), EtOH, reflux	5	98 <sup>b</sup>

<sup>a</sup> Isolated yields. <sup>b</sup> This work.

different polar and non-polar solvents including toluene,  $\text{CH}_3\text{CN}$ ,  $\text{MeOH}$ ,  $\text{EtOH}$ ,  $\text{H}_2\text{O}$ ,  $\text{DMSO}$ , and also under solvent-free conditions. It was found that the best result was obtained in refluxed ethanol. The reaction temperature was also affected and the best result was observed at reflux conditions in ethanol. Finally, according to the mentioned results, the use of 0.004 g of  $\text{Fe}_3\text{O}_4@\text{FSM-16-SO}_3/\text{IL}$ , and  $\text{EtOH}$  solvent at reflux conditions was selected as the optimum conditions (Table 1). Subsequently, different aryl aldehydes containing electron-donating and electron-accepting groups were used to prepare polyhydroquinoline derivatives. As shown in Table 2, the products were successfully obtained in good to excellent yields.

As shown in Scheme 3, a mechanism for the synthesis of polyhydroquinoline derivatives (**5a–i**) via the Hantzsch reaction in the presence of  $\text{Fe}_3\text{O}_4@\text{FSM-16-SO}_3/\text{IL}$  nanocatalyst is proposed. Firstly, dimedone and aldehyde were activated by the base site and the acidic sites of the nanocatalyst, respectively. Then, the Knoevenagel condensation was performed by the nucleophilic addition of active methylene of dimedone to the activated carbonyl group of aldehyde to produce intermediate **I**. On the other, intermediate **II** (enamine) was formed through the condensation of ammonia with catalyst-activated ethyl acetoacetate. Then, intermediate **I** performed a Michael addition with enamine to give intermediate **III**. Finally, the final product was synthesized by intramolecular cyclization of **III** followed by  $\text{H}_2\text{O}$  elimination.

### 3.3. Efficiency of the catalyst

In order to investigate the heterogeneous or homogeneous nature of the  $\text{Fe}_3\text{O}_4@\text{FSM-16-SO}_3/\text{IL}$  nanocatalyst, a leaching test was performed under optimum reaction conditions in the model reaction. To this end, the catalyst was separated by an external magnet after almost 50% of the reaction had taken place. Next, the residue of the reaction mixture under optimum conditions was stirred, but no significant progress in the reaction was observed. The result of this test confirms that the catalyst acts heterogeneously. To evaluate the recyclability and reusability of the  $\text{Fe}_3\text{O}_4@\text{FSM-16-SO}_3/\text{IL}$  magnetic solid acid nanocatalyst, the reaction of benzaldehyde, dimedone, ethyl acetoacetate, ammonium acetate under optimum reaction conditions was carried. After completion of the reaction process, the catalyst was separated by the external magnetic field and was washed with ethanol, dried, and reused six times without any significant decrease in its catalytic activity (Fig. 10).

In the following, the FT-IR spectrum of the recovered  $\text{Fe}_3\text{O}_4@\text{FSM-16-SO}_3/\text{IL}$  nanocatalyst is shown in Fig. 11. This analysis confirms the high strength and stability of the catalyst structure after recycling. Also, the XRD diffraction pattern of the recovered catalyst was analyzed. As shown, the relative intensity and position of all peaks, and the structural stability were confirmed (Fig. 12).

Next, the comparison of the performance of the  $\text{Fe}_3\text{O}_4@\text{FSM-16-SO}_3/\text{IL}$  catalyst was investigated with other reported catalysts for the synthesis of polyhydroquinoline derivatives was investigated. Based on the results in Table 3, the  $\text{Fe}_3\text{O}_4@\text{FSM-16-SO}_3/\text{IL}$  nanocatalyst is comparable with other catalysts in terms of recycling times and reusability, short reaction time, amount of the catalyst, reaction temperature, type of solvent, and product yield.

## 4. Conclusions

This study presents a new ionic liquid based on magnetic FSM-16 nanocomposite and its catalytic application in the synthesis of polyhydroquinoline derivatives. The FE-SEM and TEM images of the  $\text{Fe}_3\text{O}_4@\text{FSM-16-SO}_3/\text{IL}$  catalyst showed a spherical morphology with a highly ordered structure. Furthermore, the XRD, TGA, EDX, and FT-IR analyses confirmed the high stability, and also the immobilization of the ionic liquid on the magnetic mesoporous framework. Also, the VSM analysis showed well the magnetic properties of this nanocomposite. Some of the remarkable advantages of this catalyst are short reaction time, excellent product yield, and chemical stability. More importantly, the catalyst can be recovered using an external magnet and reused 6 times without significant loss of catalytic activity.

## Conflicts of interest

There are no conflicts to declare.

## Acknowledgements

The authors gratefully acknowledge the partial support of this work by Yasouj University, Iran.

## Notes and references

1 P. Kaur and H. K. Chopra, *ChemistrySelect*, 2020, **5**, 12057.



2 G. Martínez-Edo, A. Balmori, I. Pontón, A. Martí del Rio and D. Sánchez-García, *Catalysts*, 2018, **8**, 617.

3 M. Ma, K. Gao, D. Zhao, X. Ma and Z. Ma, *J. Environ. Chem. Eng.*, 2022, **10**, 106937.

4 M. Hajjami, L. Shiri and A. Jahanbakhshi, *Appl. Organomet. Chem.*, 2015, **29**, 668.

5 F. Tavakoli, M. Mamaghani and M. Sheykhan, *Appl. Organomet. Chem.*, 2019, **33**, 5083.

6 M. Samari, S. Zinadini, A. A. Zinatizadeh, M. Jafarzadeh and F. Gholami, *Appl. Water Sci.*, 2022, **12**, 263.

7 T. Yamamoto, T. Tanaka, T. Funabiki and S. Yoshida, *J. Phys. Chem. B*, 1998, **102**, 5830.

8 H. Araki, A. Fukuoka, Y. Sakamoto, S. Inagaki, N. Sugimoto, Y. Fukushima and M. Ichikawa, *J. Mol. Catal. A: Chem.*, 2003, **199**, 95.

9 A. Matsumoto, T. Sasaki, N. Nishimiya and K. Tsutsumi, *Colloids Surf. A*, 2002, **203**, 185.

10 T. Yanagisawa, T. Shimizu, K. Kuroda and C. Kato, *Bull. Chem. Soc. Jpn.*, 1990, **63**, 988.

11 S. Inagaki, A. Koiwai, N. Suzuki, Y. Fukushima and K. Kuroda, *Bull. Chem. Soc. Jpn.*, 1996, **69**, 1449.

12 A. Jahanbakhshi, M. Farahi, B. Karami and I. Sedighimehr, *RSC Adv.*, 2022, **12**, 34325.

13 S. Hashemi-Uderji, M. Abdollahi-Alibeik and R. Ranjbar-Karimi, *J. Porous Mater.*, 2019, **26**, 467.

14 M. Samari, S. Zinadini, A. A. Zinatizadeh, M. Jafarzadeh and F. Gholami, *J. Environ. Chem. Eng.*, 2021, **9**, 105386.

15 S. Hashemi-Uderji, M. Abdollahi-Alibeik and R. Ranjbar-Karimi, *Main Group Met. Chem.*, 2018, **41**, 91.

16 F. Gholamian, M. Hajjami and A. M. Sanati, *Silicon*, 2020, **12**, 2121.

17 M. B. Gawande, R. Luque and R. Zboril, *ChemCatChem*, 2014, **6**, 3312.

18 H. Kefayati, M. Golshekan, S. Shariati and M. Bagheri, *Chin. J. Catal.*, 2015, **36**, 572.

19 R. Abu-Reziq, H. Alper, D. Wang and M. L. Post, *J. Am. Chem. Soc.*, 2006, **128**, 5279.

20 A. Alizadeh, M. M. Khodaei, M. Beygadeh, D. Kordestani and M. Feyzi, *Bull. Korean Chem. Soc.*, 2012, **33**, 2546.

21 S. Shylesh, V. Schünemann and W. R. Thiel, *Angew. Chem., Int. Ed. Engl.*, 2010, **49**, 3428.

22 R. Bakhshali-Dehkordi, M. A. Ghasemzadeh and J. Safaei-Ghomí, *Appl. Organomet. Chem.*, 2020, **34**, 5721.

23 A. C. Barsanti, C. Chiappe, T. Ghilardi and C. S. Pomelli, *RSC Adv.*, 2014, **4**, 38848.

24 M. Taheri, M. Ghiasi, A. Moheb and A. Shchukarev, *Appl. Organomet. Chem.*, 2019, **33**, 5012.

25 B. Karimi, M. Tavakolian, M. Akbari and F. Mansouri, *ChemCatChem*, 2018, **10**, 3173.

26 R. D. Noble and D. L. Gin, *J. Membr. Sci.*, 2011, **369**, 1.

27 A. Basaiahgari, S. K. Yadav and R. L. Gardas, *Pure Appl. Chem.*, 2019, **91**, 1279.

28 M. Yoshizawa, M. Hirao, K. Ito-Akita and H. Ohno, *J. Mater. Chem.*, 2001, **11**, 1057.

29 K. V. Wagh and B. M. Bhanage, *ACS Sustain. Chem. Eng.*, 2016, **4**, 445.

30 J. Li and Z. Guo, *ACS Sustain. Chem. Eng.*, 2017, **5**, 1237.

31 G. A. Kraus and T. A. Guney, *Green Chem.*, 2012, **14**, 1593.

32 S. Yin, J. Sun, B. Liu and Z. Zhang, *J. Mater. Chem. A*, 2015, **3**, 4992.

33 B. Mirhosseini-Eshkevari, M. A. Ghasemzadeh, M. Esnaashari and S. T. Ganjali, *RSC Adv.*, 2021, **11**, 364.

34 K. Ojaghi Aghbash, N. Noroozi Pesyan and H. Batmani, *Appl. Organomet. Chem.*, 2019, **33**, 5227.

35 S. Abaeenezadeh, D. Elhamifar, M. Norouzi and M. Shaker, *Appl. Organomet. Chem.*, 2019, **33**, 4862.

36 Y. Hu, L. Yang and X. Liu, *Molecules*, 2023, **28**, 242.

37 M. Khorasani, B. Karimi and H. Vali, *React. Chem. Eng.*, 2022, **7**, 2618.

38 R. Pourhasan Kisomi, F. Shirini and M. Golshekan, *Appl. Organomet. Chem.*, 2021, **35**, 6212.

39 H. Kefayati, S. J. Bazargard, P. Vejdaneft, S. Shariati and A. M. Kohankar, *Dyes Pigm.*, 2016, **125**, 309.

40 M. Norouzi and D. Elhamifar, *Composites, Part B*, 2019, **176**, 107308.

41 S. Rostamnia and A. Hassankhani, *Synlett*, 2014, **25**, 2753.

42 R. Ghorbani-Vaghei and V. Izadkhah, *Appl. Organomet. Chem.*, 2018, **32**, 4025.

43 Y. Wu, L. Ma, Z. Song, S. Dong, Z. Guo, J. Wang and Y. Zhou, *Carbon Neutrality*, 2023, **2**, 1.

44 G. Wu, S. Dong, P. Fu, Q. Yue, Y. Zhuo and J. Wang, *Green Chem.*, 2022, **24**, 3433.

45 G. Li, S. Dong, P. Fu, Q. Yue, Y. Zhou and J. Wang, *Chem. Eng.*, 2020, **390**, 124652.

46 N. H. Sapariya, B. K. Vaghasiya, R. P. Thummar, R. D. Kamani, K. H. Patel, P. Thakor, A. Ray and D. K. Raval, *New J. Chem.*, 2017, **41**, 10686.

47 R. R. Raslan, S. A. Hessein, S. A. Fouad and N. A. Shmiess, *J. Heterocycl. Chem.*, 2022, **59**, 832.

48 A. M. Aqeel, L. Zhenling, P. Wan-Xi and G. Caixia, *Catal. Lett.*, 2020, **150**, 683.

49 A. Barzkar and A. S. Beni, *RSC Adv.*, 2020, **10**, 41703.

50 L. M. Wang, J. Sheng, L. Zhang, J. W. Han, Z. Y. Fan, H. Tian and C. T. Qian, *Tetrahedron*, 2005, **61**, 1539.

51 M. Kazemi and M. Mohammadi, *Appl. Organomet. Chem.*, 2020, **34**, 5400.

52 M. Farahi, B. Karami, I. Sedighimehr and H. M. Tanuraghaj, *Chin. Chem. Lett.*, 2014, **25**, 1580.

53 M. Farahi, F. Tamaddon, B. Karami and S. Pasdar, *Tetrahedron Lett.*, 2015, **56**, 1887.

54 A. Jahanbakhshi and M. Farahi, *Arabian J. Chem.*, 2022, **15**, 104311.

55 S. Akrami, B. Karami and M. Farahi, *RSC Adv.*, 2017, **7**, 34315.

56 A. Jahanbakhshi, M. Farahi and Y. Aghajani, *Acta Chim. Slov.*, 2022, **69**, 837.

57 J. E. Gholtash and M. Farahi, *RSC Adv.*, 2018, **8**, 40962.

58 R. Keshavarz and M. Farahi, *RSC Adv.*, 2022, **12**, 3584.

59 K. Kondamudi, P. Elavarasan, P. J. Dyson and S. Upadhyayula, *J. Mol. Catal. A: Chem.*, 2010, **321**, 34.

60 G. D. Rao, S. Nagakalyan and G. K. Prasad, *RSC Adv.*, 2017, **7**, 3611.



61 B. Maleki, H. Alinezhad, H. Atharifar, R. Tayebee and A. V. Mofrad, *Org. Prep. Proced. Int.*, 2019, **51**, 301.

62 S. Mondal, B. C. Patra and A. Bhaumik, *ChemCatChem*, 2017, **9**, 1469.

63 S. K. Das, S. Mondal, S. Chatterjee and A. Bhaumik, *ChemCatChem*, 2018, **10**, 2488.

64 A. Davoodnia, M. Khashi and N. Tavakoli-Hoseini, *Chin. J. Catal.*, 2013, **34**, 1173.

65 M. Hajjami and B. Tahmasbi, *RSC Adv.*, 2015, **5**, 59194.

